DIC to evaluate a model composite system cracking due to CTE mismatch

Igor Paganotto Zago, Rafael Vargas, Vinicius Fiocco Sciuti, Rodrigo Bresciani Canto, Ricardo Afonso Angélico

DIC to evaluate a model composite system cracking due to CTE mismatch

Igor Paganotto Zago[1], Rafael Vargas[1,2], Vinícius Fiocco Sciuti[3], Rodrigo Bresciani Canto[3], Ricardo Afonso Angélico[4]

Federal University of São Carlos, Graduate Program in Materials Science and Engineering - PPGCEM, São Carlos, Brazil

Université Paris-Saclay, CentraleSupélec, ENS Paris-Saclay, CNRS, LMPS - Laboratoire de Mécanique Paris-Saclay, Gif-sur-Yvette, France

Federal University of São Carlos, Department of Material Engineering - DEMA, Rod. Washington Luiz, km 235, São Carlos, Brazil

University of São Paulo, São Carlos School of Engineering, Department of Aeronautical Engineering, Av. João Dagnone, 1100 - Santa Angelina, São Carlos, Brazil

Abstract

Coefficient of thermal expansion (CTE) mismatch in composites under temperature variation can lead to the system cracking. In this study, Digital Image Correlation (DIC) was used to investigate this phenomenon in a model composite system (MCS) composed of a single cylindrical inclusion into a ceramic mortar matrix. Temperature variation experiments assisted by DIC were conducted to evaluate the CTE mismatch of the MCS and to observe its cracking. An analytical model was used to fit the experimental radial displacement field of the MCS, which allowed the computation of the inelastic maximum principal strain field, highlighting the radial crack pattern. The crack initiation and propagation were evaluated via damaged elements in the interface region and the computation of the average Mean Crack Opening Displacement and Surface Crack Density for crack regions. This methodology is appliable for a single inclusion MCS, with improvement perspectives for application in multiple inclusions MCS.

Keywords: Crack pattern, Model material, Thermomechanical behavior, Digital Image Correlation, Thermal expansion.

1. Introduction

The development of composite materials is intrinsically related to combining materials that lead to enhanced properties (e.g., mechanical, thermal, electromagnetic, biodegradability, optical) for a given engineering application. The more straightforward composite system involves dispersed and continuous phases that interact and transfer loads through interface regions [1]. Therefore, the macroscopic properties of composite systems are a consequence of the interaction among the phases [2, 3]. Sometimes, such interaction may benefit a specific property while another is detrimentally affected. For instance, composite systems formed by phases with different coefficients of thermal expansion are subjected to stresses during temperature variation, which can lead to material failure [4–7]. Differently, a system designed to increase thermal insulation properties could benefit from the existence of cracks and other defects to the detriment of some mechanical properties, such as stiffness and strength [8–10]. Besides, many composites manufacturing involves temperature variations steps that can affect the composite effective properties in reason of CTE mismatch of its phases [11–15]. Thus, comprehending the phases interaction is fundamental to better understanding mechanical behavior when the material system is subjected to temperature variations [6, 7, 11, 16].

Cracks due to phase's thermal expansion mismatch are an essential subject in the development of high-performance Ceramic Matrix Composites (CMCs) like those used in aerospace, automotive, and energy applications [17–20]. Also, in the processing routes of some composites, for instance, Chemical Vapor Infiltration (CVI), Chemical Vapor Deposition (CVD), and Melt-Infiltration (MI) process, where it is not unusual for the appearance of cracks or Thermal Residual Stress (TRS) in the material after cooling [21–23]. Therefore, cracks in composites can originate from residual thermal stress in the processing and thermal stress under in-service conditions [24]. The experimental research presented in this paper brings data regarding a Model Composite System (MCS) cracked due to a CTE mismatch of its constituents during a heating process.

The cracking in MCS has been studied using analytical, computational, and experimental approaches. The first two enable determining the strain and stress fields when applying thermal loads, which gives valuable information for understanding the thermomechanical behavior of the system [25–28]. Experimental approaches have investigated the appearance of cracks in composite systems due to temperature variation [6, 29], or evaluated macroscopic system parameters, such as Young modulus history [12]. These approaches bring essential insights into cracks induced by composite system's thermomechanical behavior and its implications for the mechanical behavior of composite materials in temperature variation applications. However, experimental local information concerning the phase interaction, such as crack nucleation and propagation, is unavailable. Experimental devices assisted by field measurement techniques can bring much more information from the experimental evaluation of composite systems [15, 30–34].

Digital image correlation (DIC) is a technique that allow the measurement of full-field displacement by comparing two images in different stages of deformation [35–37]. The technique has advantages such as the field information it provides, and its application is non-invasive, avoiding measurement disturbances due to instrumentation contact with the sample or the test equipment. The full-field data, provided by the technique, brings valuable information about observed phenomena. In that way, it can help to identify several properties or behaviors of tested materials and help to evaluate other parameters of interest like the crack path [31, 38].

MCS are materials where the phases' shape and constituents, and also the system volume fraction (ϕ) are chosen for study purposes. Using MCS to simplify the study makes it possible to avoid secondary phenomena that could impact the results. Several studies use MCS to analyze the stresses among phases in heterogeneous materials, crack nucleation, and its propagation, making use of several strategies in the material design to enable the observation of such phenomena [12, 21, 25, 39, 40].

The present study aims to bring a new approach to analyze the cracking induced by the product $\Delta\alpha\Delta T$ in a MCS, where $\Delta\alpha$ and ΔT corresponds to a coefficient of thermal expansion (CTE) mismatch and a temperature variation, respectively. The MCS studied consists of a single inclusion into a matrix, and the results are deemed to be valid for systems with a low volume fraction ($\phi \leq 10\%$). DIC technique is used to evaluate the displacement field in the inclusion and matrix and to enhance the experimental data to investigate their interaction. The proposed methodology enables observing and analyzing a MCS with a single cylindrical inclusion surrounded by a matrix while prescribing a temperature variation. An analytical model is also used to further comprehend the phenomena. The results in this paper show an improvement in the analysis of CTE mismatch in composite systems by presenting full-field *in*

situ evolution data of the phases' interaction during a temperature variation experiment. The conducted investigation evaluates only the effects of thermal loading in the system. Most of the literature regarding this subject is related to how the Thermal Residual Stress (TRS) and damage - produced in the cooling process of some composites manufacturing - will affect the mechanical response of composites in in-service conditions. The present study evaluates experimentally the damage induced by a CTE mismatch in composites using non-intrusive measurement techniques.

2. Heterogeneous materials submitted to a temperature variation

The research about stresses around a particle inclusion induced by a temperature variation, especially in glass matrix composites, has been a current issue since the 60s. Selsing [4] proposed an analytical model based on the formulation of thick-walled spherical shells for the interfacial radial stress calculus of a single spherical inclusion embedded in an infinity matrix. In his model the interfacial pressure $p_{(i/m)}$ due to a temperature variation ΔT is given by:

$$p_{(i/m)} = \frac{\Delta\alpha\,\Delta T}{\dfrac{1+\nu_M}{2E_M} + \dfrac{1-2\nu_I}{E_I}} \tag{1}$$

where E is the modulus of elasticity, ν is the Poisson's ratio, $\Delta\alpha$ is the coefficient of thermal expansion mismatch, i.e. $\Delta\alpha = \alpha_I - \alpha_M$. Subscripts m and i denote the matrix and inclusion domains, while M and I the matrix and inclusion material properties, respectively.

Depending on the interfacial stress signs, different crack patterns are observed. These stresses depend on the phases CTE relation and the increase or decrease of temperature. In all situations, the radial stress σ_{rr} is continuous from the inclusion to the matrix. In contrast, the tangential stress $\sigma_{\theta\theta}$ will have the same magnitude in the inclusion and matrix interface but with opposite signals. For a model like Selsing's, the radial stress has twice the magnitude of the tangential stress ($p_{(i/m)} = -\sigma_{rr} = 2\,\sigma_{\theta\theta}$). The cracks in systems like these, are a result of tensile stresses; if $\Delta\alpha\,\Delta T > 0$, the cracks will be radial once tangential tensile stress arises in the interface. For $\Delta\alpha\,\Delta T < 0$, the material will present circumferential cracks once radial tensile stress arises in the interface. These crack patterns are illustrated in Figure 1 and have been reported in several articles [6, 7, 12, 16, 40].

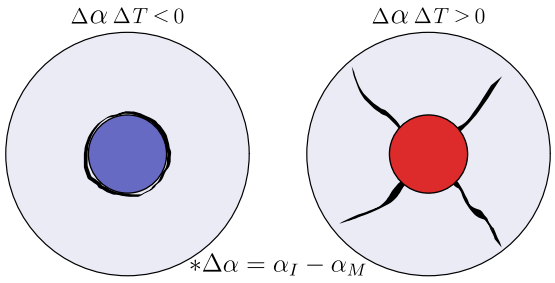

Figure 1: Expected crack pattern for a single inclusion embedded in a matrix as result of a temperature variation in a system with CTE misfit. [3].

From Selsing's equation, an abacus was designed (Figure 2). The ordinate values refer to the denominator of Equation (1), related to the inclusion and matrix elastic parameters (E_I, ν_I, E_M, ν_M) in the interfacial stress, and the

abscissas refer to the CTE mismatch between the phases. Finally, the isovalues and colormap present the resultant interfacial stress values per degree of temperature increase. These stress values are computed considering a single spherical inclusion into an infinite matrix and a perfect contact in the phases' interface. Furthermore, it is assumed that the material properties are not temperature-dependent. Since tangential stress components change the sign at the interface, it was established that the reference of signs is the matrix domain, where cracks appear. The diagram displayed in Figure 2 allows the visualization of the crack inductive stress (tensile stress) per °C of temperature variation for a given binary material system with spherical inclusions and low volume fraction ($\phi \leq 10$ %). Examples of some glass matrix model materials with spherical alumina inclusions present in the literature are shown in Figure 2 [4, 12]. Considering a positive ΔT, the warm hues of Figure 2 represent $2\sigma_{\theta\theta}$ values that result in a radial crack pattern, as shown in Figure 1 for $\Delta\alpha\,\Delta T > 0$, while the cold hues of Figure 2 represent σ_{rr} values that result in an orthoradial crack pattern, as the one presented in Figure 1 for $\Delta\alpha\,\Delta T < 0$. It is worth noting that the opposite behavior occurs for a negative temperature variation.

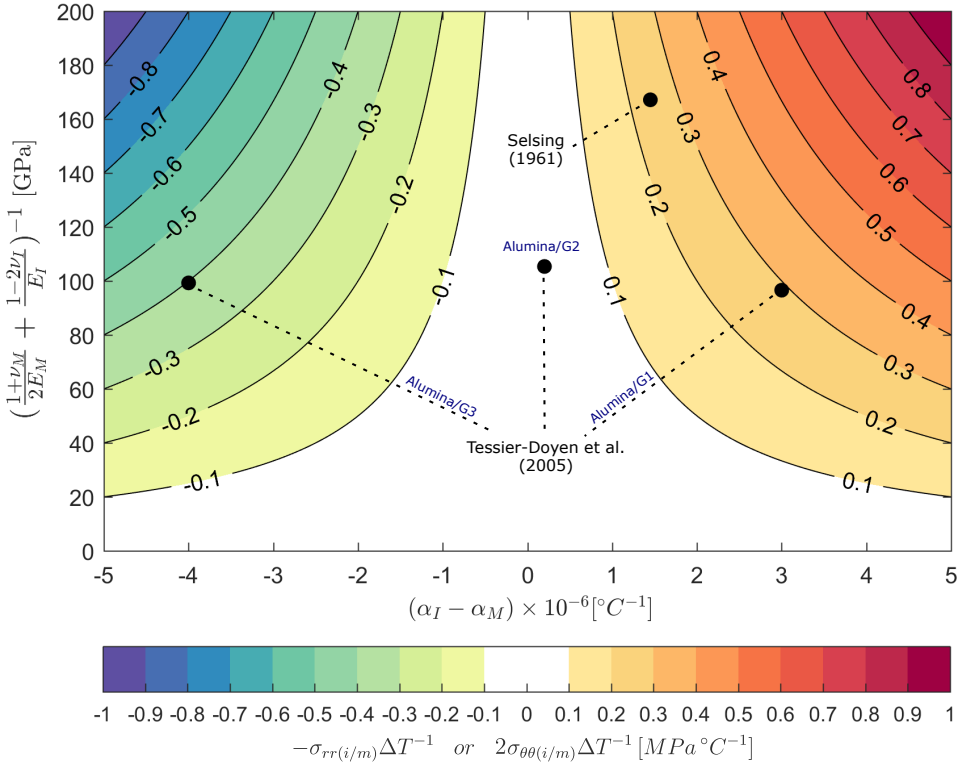

Figure 2: Interfacial stress caused by temperature increase for a spherical inclusion into an infinite matrix as a function of the inclusion and matrix elastic parameters, and the mismatch between the phases ($\alpha_I - \alpha_M$), for the matrix domain [4, 12]. This diagram is a graphical display based on Equation 1, where the interfacial stress per °C of a biphasic system can be represented by a point. The vertical axis contains the mechanical properties relation, and the horizontal axis their CTE mismatch. For example, for Selsing's system, the tangential interfacial stress will increase for each degree Celsius of temperature in ∼0.25 MPa.

The principles presented so far are proper for approaches like single inclusion systems or low volume fractions

($\phi \leq 10$ %). For higher volume fraction systems ($\phi > 10\%$), the stresses for a given point in the matrix are influenced by a cluster of inclusions surrounding it. Therefore, for high-volume fractions, complex crack patterns can be observed. In Tessier-Doyen's work, for example, inter-inclusion cracks were observed, and Joliff et al. investigated experimental and numerically these inter-inclusion cracks and proposed that they were caused by the sample's pressing and sintering processes [39]. Luchini et al. [41] verified that not always the matrix inclusion interface is the most energetic area for surface formation. By numerical simulations, they observed that the region between two inclusions will be more energetic than the interface for high volume fractions, which is another possible explanation for the inter-inclusion cracks observed in Tessier-Doyen's experiments.

Several studies also investigated the CTE mismatch for a cylindrical fiber embedded into a matrix. For this system, the radial stress has the same magnitude as the tangential stress ($\sigma_{rr} = \sigma_{\theta\theta}$), considering that, in the inclusions domain $\sigma_{rr} = \sigma_{\theta\theta}$ and in the matrix domain $\sigma_{rr} = -\sigma_{\theta\theta}$. Bobet and Lamon [11, 21] described a cylindrical solution for the calculus of the Thermal Residual Stress (TRS) of three concentric phases - a fiber, interphase and matrix - for a temperature variation process, showing that different interphases and the interphase thickness modify the resultant stress profile. Folias et al. [7] also developed an analytical study to predict the crack initiation in fiber composite systems due to CTE mismatch, investigating critical effects caused by the application of loads in the transverse direction of the fibers in systems with residual thermal stress. They have also shown the possibility to use a fracture criterion to predict a local crack initiation.

3. Cylindrical inclusion surrounded by an infinite matrix

The model described herein represents a single cylindrical inclusion of radius r_i into an infinite matrix for a system with small thickness submitted to a temperature variation ΔT (Figure 3). For the mentioned problem, it is convenient to describe the variables of interest in cylindrical coordinates, with the origin of the coordinate system being the center of the inclusion. Considering the problem as axisymmetric, the radial and tangential displacements, u_r and u_θ respectively, are given by:

$$u_r(r,\theta) = Ar + \frac{B}{r}; \quad u_\theta(r,\theta) = 0 \tag{2}$$

where A and B are constants determined from boundary conditions.

The constants A and B must be identified for the inclusion and matrix domains regarding the problem boundary conditions. The first boundary condition is that the inclusion center is fixed ($u_r(r = 0) = 0$). A perfect interface between inclusion and matrix was also assumed, *i.e.*, $u_{r_i}(r_i) - u_{r_m}(r_i) = 0$ and ($\sigma_{rr_i}(r_i) = \sigma_{rr_m}(r_i)$). Further, only thermal loads are considered, therefore, when the radius tends to infinity, the radial stress σ_{rr} tends to zero ($\lim_{r\to\infty} \sigma_{rr}(r) = 0$), once the only stresses induced in the system originate in the interface and decay in the matrix domain whereas the radial coordinate increases.

For an isotropic material subjected to a temperature variation, its total strain ($\boldsymbol{\varepsilon}$) results from the sum of elastic ($\boldsymbol{\varepsilon^e}$) and thermal ($\boldsymbol{\varepsilon^t}$) strains. Its strain tensor is described as:

$$\boldsymbol{\varepsilon} = \boldsymbol{\varepsilon}^e + \boldsymbol{\varepsilon^t} \tag{3}$$

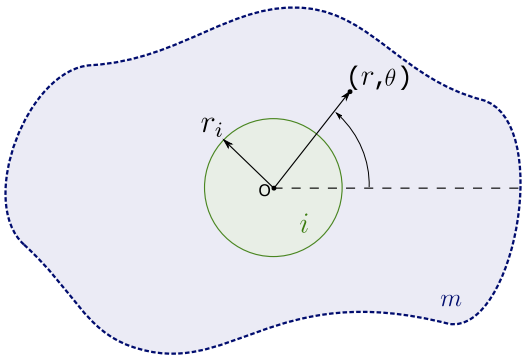

Figure 3: Cylindrical inclusion (i) into an infinite matrix (m).

where the thermal strain is given by $\boldsymbol{\varepsilon}^t = \mathbf{I}\,\alpha\,\Delta T$.

Considering a plane stress state, and applying the boundary conditions mentioned above, it is possible to express the displacement field as:

$$u_r(r) = \begin{cases} A_i\, r & \text{if } r \in \Omega_i \equiv [0, r_i] \\ A_m\, r + \dfrac{B_m}{r} & \text{if } r \in \Omega_m \equiv [r_i, \infty) \end{cases} \tag{4}$$

where the constants A_i, A_m and B_m are:

$$A_i = \frac{(Z_I\,\alpha_I + \mu_M\,\alpha_M)\,\Delta T}{Z_I + \mu_M} \tag{5}$$

$$A_m = \alpha_M\,\Delta T \tag{6}$$

$$B_m = \left[\frac{Z_I\,(\alpha_I - \alpha_M)\,\Delta T}{Zi + \mu_M}\right] r_i^2 \tag{7}$$

and $Z_I = \lambda_I + \mu_I - \dfrac{\lambda_I^2}{\lambda_I + 2\mu_I}$, being λ and μ the first and second Lamé parameters, respectively. It is essential to highlight that the model parameters can be related to each other using the inclusion radius as:

$$A_i - A_m - \frac{B_m}{r_i^2} = 0 \tag{8}$$

A physical interpretation of the model parameters on the radial displacement can be seen in Figure 4. The solution has three parameters. Inside the inclusion domain, the solution is linear and its slope is given by the parameter A_i. When distant from the inclusion, the slope is governed by the parameter A_m, which corresponds only to the thermal expansion of the matrix. The transition region, close to the inclusion, is governed by the parameter B_m and decays in magnitude with $1/r$ factor. Since B_m can be written in terms of A_i, A_m and r_i, the extension of the transition region depends on the inclusion radius.

For the plane stress condition, it is also possible to evaluate the stresses via the solution of the analytical model, being that in the model, the highest values of stress will occur in the interface. Therefore, it is also in this region that crack nucleation would be expected. The interfacial radial ($\sigma_{rr}(r_i)$) and tangential ($\sigma_{\theta\theta}(r_i)$) stresses for the matrix domain can be calculated as:

$$\sigma_{\theta\theta}(r_i) = -\sigma_{rr}(r_i) = \frac{2\,Z_I\,\mu_M(\alpha_I - \alpha_M)\Delta T}{Z_I + \mu_M} \tag{9}$$

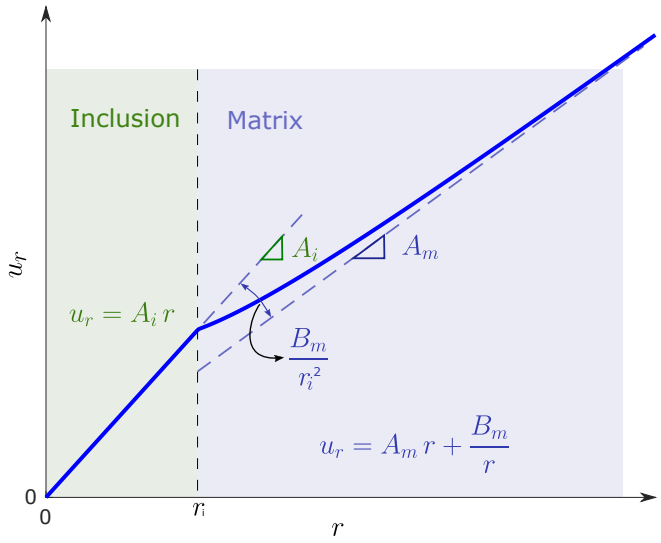

Figure 4: Interpretation of the model parameters. The radial displacement in the MCS is governed by the A_i parameter, into the inclusion, while A_m and B_m in the matrix.

4. Model composite manufacture

In the present study, the model composite system (MCS) consists of a 12.7 mm diameter cylindrical inclusion of C360 brass surrounded by an alumina mortar shaped as a disk with a diameter of 140 mm. The ratio between the inclusion and the specimen's outer diameter is 1:11, and the specimen has 8 mm in thickness. The inclusion material was selected to give a high CTE mismatch to the system and for its elevated elastic modulus, because the higher the CTE mismatch between the phases and elastic modulus of the phases, the higher the interfacial stress between them. The in-plane dimension of the inclusion is larger than the out-of-plane (8 mm), and a plane stress state approach is thus considered as adequate to describe the problem. The geometrical configuration was designed to allow a measurable displacement field using the camera setup (described in Section 5), and to achieve a stress level that leads to the matrix fracture.

The MCS manufacturing used a silicone mold, where an internal steel template ensured the inclusion positioning. The inclusion has a centered face 2 mm diameter through-hole used to fix it to the template with a screw and a nut, as seen in Figure 5. The disc template was covered with a plastic film to facilitate the demolding process. The alumina mortar matrix was produced by gel casting, where a wet powder mix of calcined alumina with a granulometry ≤ 180 μm and colloidal silica was prepared in a weight proportion of 1:3.5. In this process, it was used a vibratory table to assist the scatter of the alumina paste in the mold cavity until the depth covers the inclusion. Then, the composite was left to dry for two days in a greenhouse at 40 °C. After that, the specimen was released from the mold and smoothly sanded to level the surface, enabling the visualization of the inclusion, and the specimen was removed from the template. The last stage was the painting of a texture in the MCS surface by using white and black sprays for high temperatures (recommended for usage up to 600 °C) to create the pattern required to apply DIC.

The matrix was only dried, not sintered, to keep the fracture strength low and achievable by the CTE mismatch.

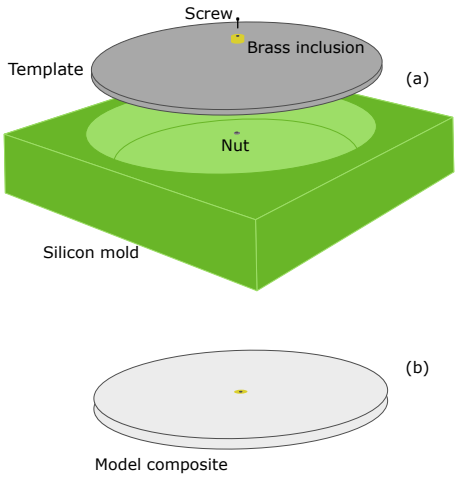

Figure 5: Model composite manufacturing: (a) assembly used for the casting; (b) MCS after cure and dry.

It is worth noting that the objective of this study is to show the use of DIC to follow the crack pattern evolution in a composite model, not to evaluate good mechanical properties in a given system.

The conceptual idea behind this model composite was to create a system that allows the full-field investigation of the phases' interaction in the radial direction of a fiber reinforced composite. The temperature increase test of this model material allows observing the cracks' initiation due to the CTE mismatch of the phases and the propagating through the matrix medium. These experimental results can assist in the development of analytical and computational fracture models for presenting a direct visualization of the phenomenon in a simple system. The material selection of the system was done by practical purposes, being that the experiment can be executed with different materials systems.

5. Experimental tests assisted by DIC

5.1. Experimental procedure

The experiments were conducted in an oven designed to allow the image acquisition of specimens during a temperature variation experiment. The oven is a cubic chamber with a 400 mm edge internally. Three borosilicate windows positioned on the top cover enable the image acquisition and illumination of the specimen inside it, as illustrated in Figure 6. The specimen was positioned facing up the cover and aligned with the main window. The heater elements are positioned in the bottom of the oven, and the small sample thickness contributes to avoid temperature gradients.

Two types of tests were performed. The first was optical dilatometry (*i.e.* dilatometry assisted by DIC) tests, which use homogeneous materials - e.g., "Matrix material" and "Inclusion material" - to identify the CTE mismatch of the phases. The second was the temperature variation of the MCS to obtain the displacement fields resultant of the interaction of the coupled phases' expansion and to observe the crack pattern, and its growth.

The specimens were positioned with no horizontal restrictions, which led to rigid body motions caused by the thermal expansion of the experimental assembly inside the oven. The experimental procedure began with the oven's

temperature being set constant for twenty minutes to homogenize its internal chamber. The initial temperature for the MCS temperature variation test was 40°C and for the dilatometry tests was 50°C. After that, the temperature increases at a rate of 1°C/min until 300°C marking the end of the experiment. It is important to highlight that the present experimental procedure consists of heating, while other works analyzed the material mechanical behavior during the cooling [4, 6, 12, 42]. The camera acquisition rate was one photograph per minute. Thirty photographs were taken to analyze the displacement uncertainty during the homogenization temperature step. The digital camera used for all experiments was a Canon Rebel T7i (24.2 Megapixels), and the camera lens was a Canon Macro Lens EF 100 mm 1:2.8 USM.

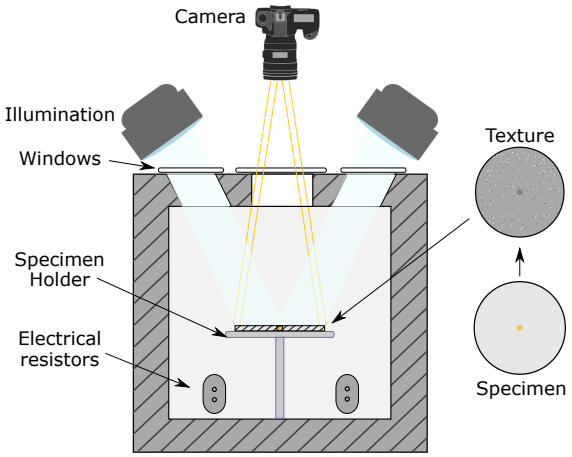

Figure 6: Oven projected to allow the conduction of temperature variation test experiments assisted by DIC.

The experimental acquisition noise can be used to assist defining the crack initiation. The DIC noise was estimated as the mean value of the standard deviation nodewise for each field of interest among the reference images taken at the initial temperature (40°C). For the MCS temperature variation experiment, values of radial displacement under 0.054 pixels (0.0338 μm) and of maximum principle strain under 0.001 are below this threshold and consequently considered as noise. This noise increases as the temperature increases due to optical distortions from heat haze. Therefore, even tough maximum principal strain values $\leq$ 0.001 should be considered noise, this does not mean that higher values should be inherently considered as cracks. A threshold value (ε^*) can be defined to point out a region considered cracked, and this value should be greater than the strain noise. Further, in order to define a threshold value in a temperature variation experiment, as the one performed herein, it must be taken into account that there are thermal and elastic strains that will increase in intensity together with the temperature. Therefore, these strains should be subtracted from the maximum principal strain field to obtain an inelastic strain field. It is interesting to highlight that such strategy is only possible due to the use of a full-field measurement techniques such as DIC.

5.2. Digital image correlation

For DIC, the surface analyzed is painted with white and black spray, creating a texture to improve the gradient and create a random speckle over the surface. Once a grayscale image is a bi-dimensional signal in which the intensity

distribution corresponds to the gray tone of each pixel, let us define a photograph of reference as f and another photograph in a deformed condition as g. The displacement field $\mathbf{u}(\mathbf{x})$ is obtained as the value that minimizes the gray level residual ϱ^2, which is given by:

$$\varrho^2 = \sum_{ROI} [g(\mathbf{x}) - f(\mathbf{x} + \mathbf{u}(\mathbf{x}))]^2 \tag{10}$$

where $\mathbf{x}$ represents the pixel position vector and ROI the region of interest.

All the DIC analyzes herein were performed in the Correli 3.0 framework [43] to measure full-field displacement and strain fields. The displacement field is discretized in 3-noded triangular finite elements shape functions υ, *i.e.* $\mathbf{u}(\mathbf{x}) = \sum_j^N \upsilon_j \, \mathbf{\Psi}_j(\mathbf{x})$, with j being the degree of freedom indexation and N the number of degrees of freedom. Therefore, the nodal displacements υ_j are the degrees of freedom used in the minimization of Equation (10), and then, displacements in the elements are linearly interpolated. From the displacement fields, the same framework also have tools to calculate the strain fields, which are shown and explored hereafter. The software calculates finite element displacements between ROIs of the analyzed photographs, resulting in the field displacement between two images.

The smaller the size of the elements, the higher the result definition, but also the higher the measure uncertainty [44]. Therefore, for the MCS it was chosen to use a more refined mesh (mean element area of 374 pixels^2) to improve crack visualization, and a coarser one for the dilatometries (mean element area of 1.638 pixels^2) to reduce uncertainties. It is important to disclose that, to a certain extent, the DIC results are mesh dependent, especially regarding the analysis of the cracks in the MCS. Table 1 presents the main parameters regarding the image acquisition of the experiments conducted and the image region analyzed.

Table 1: DIC hardware and ROI parameters

Camera	Canon Eos Rebel T7i
Definition	6024×4020 pixels (Bayer pixels)
Color filter	Bayer
Gray Levels amplitude	14 bits
Lens	Canon Macro Lens EF 100 mm
Aperture	$f/29$
Field of view (ROI)	2800 mm^2 (circular area)
Image scale	16 μm/pixel
Image acquisition rate	1 min^{-1}
Exposure time	1/3 s
Patterning technique	sprayed black and white paint

There are several challenges to deal with when conducting experiments in high temperatures. With the performing of DIC-assisted experiments, these challenges become even more significant when considering the implications that elevated temperatures and temperature variation bring to image acquisition. Heat haze and the expansion of all parts inside the oven must be considered to achieve more trustworthy results from such experiments. Also, the texture must not change color or vanish during the experiment.

Heat hazes are one of the most common issues in image acquisition in experiments with temperature variation [45–47]. This phenomenon results from temperature fluctuations inside the oven, creating image distortions caused by refraction and can compromise the results from DIC analysis [45–48]. Strategies can be adopted to reduce this phenomenon or minimize its effects, such as enhancing the oven homogeneity and increasing the exposition time in the image capture to gather a temporal average and smoothing out high-frequency oscillations. The exposure time of 1/3 s was the highest possible for the present setup to obtain a reasonable dynamic range (distribution of intensity) to perform the DIC analysis.

For the methodology used in this paper, it was essential to identify and remove rigid body displacements to apply the strategies that will be discussed. Further, It was also used a contrast and luminosity correction element wise to help the image correlation, once the luminosity inside the oven is affected by heat haze caused by the temperature increase [37, 49].

6. Results

6.1. Evaluation of the CTE mismatch

Optical dilatometry tests were conducted to evaluate the CTE mismatch of the phases. The temperature variation experiments provided the displacement fields, whose gradients are the thermal strain fields. The mean thermal strain fields for the brass and alumina specimens were fitted using a homogeneous second-order polynomial, being, ε_a and ε_b, the fitted polynomials for the alumina and brass, respectively.

$$\varepsilon_a = 4.3251^{-08}\Delta T^2 + 5.4729^{-06}\Delta T \tag{11}$$

$$\varepsilon_b = 4.7467^{-08}\Delta T^2 + 2.1587^{-05}\Delta T \tag{12}$$

Figure 7 (a) shows the results for the thermal strain evolution measured versus temperature variation. The CTE difference between the phases ($\Delta\alpha$) at 50°C is 16.12×10^{-6} and grows linearly to 17.17×10^{-6} at 300°C (Figure 7 (b)). Due to the experimental setup, the displacement fields attained, and consequently, the CTEs, have a parasite increment from the out-of-plane motion of the sample [50]. This out-of-plane motion results from the sample holder support rods of stainless steel. However, since the experiments have the same procedure, the parasite out-of-plane displacement was similar, and therefore, the CTE mismatch can be considered a valid evaluation.

6.2. Full-field results and model fitting

The radial (u_r) and orthoradial (u_θ) displacement fields obtained from DIC analysis are shown in Figure 8. These fields are presented to 50, 150, and 250 °C of temperature variation. The 50 °C temperature variation snapshots show small values of displacement and no field discontinuities were found. For 150 °C of temperature variation, there is a clear difference in the radial displacement magnitudes for the inclusion and matrix, a visible radial gradient. Further, four major discontinuities (*i.e.* neighbor regions with extreme difference in the values of displacement) appear in the tangential displacement field, indicating the existence of cracks. At the maximum temperature variation (250 °C), the

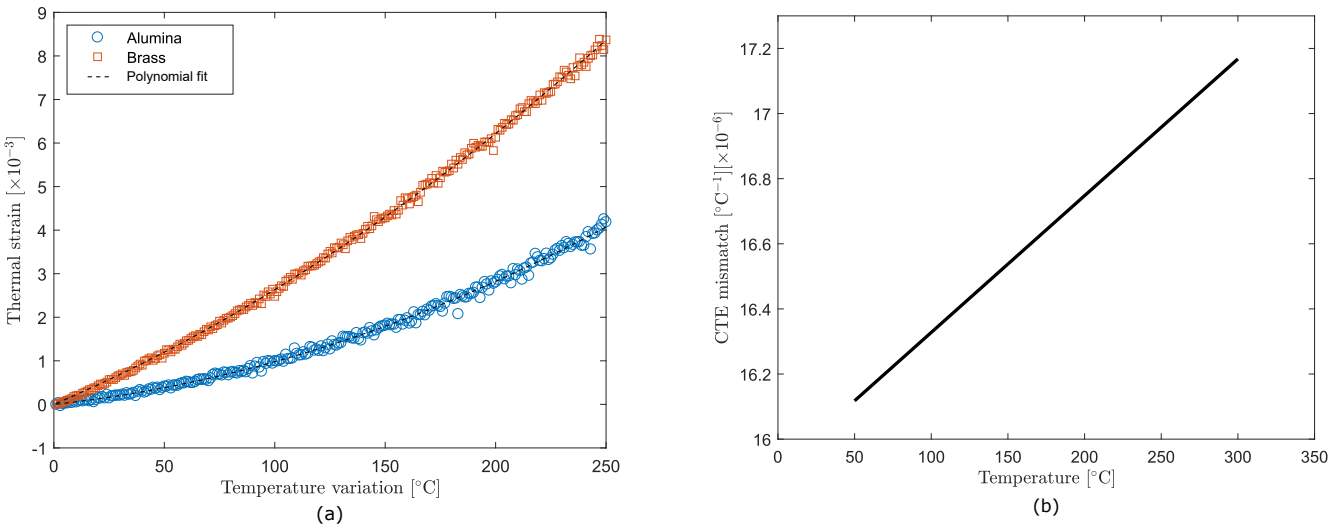

Figure 7: Dilatometry tests results: (a) alumina and brass thermal strain evolution for a temperature variation of 0 to 250°C attained via optical dilatometry; (b) coefficient of thermal expansion (CTE) mismatch between alumina and brass from 50 to 300°C.

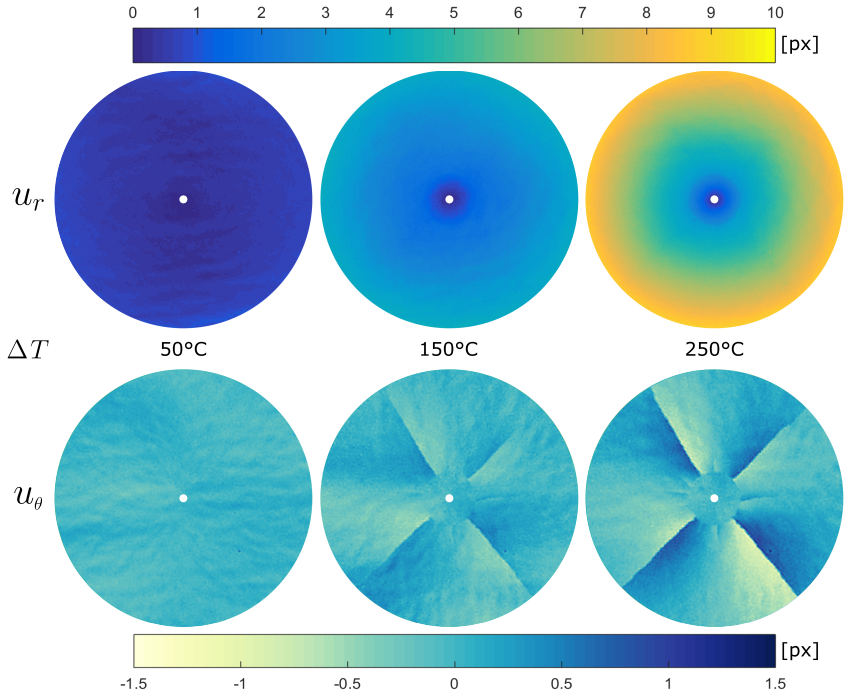

Figure 8: Evolution of the radial (u_r) and tangential (u_θ) displacement fields for temperature variations of 50, 150 and 250 °C. In this experiment 1 pixel of displacement corresponds to 16 μm.

radial displacement increases and reaches 10 pixels (160 μm) of displacement in the ROI limits. The discontinuities presented in the tangential displacement field are intensified, and new ones appear almost in the bisector of the previous.

A more straightforward way to observe the system's cracking is the maximum principal strain field [32], as seen

in Figure 9. In the temperature variation of 50 °C, there are no contrasting strain magnitudes, except for one region where a pore appeared in the specimen surface in the southeast region during the experiment. At $\Delta T = 150$ °C, four prominent cracks forming an "X" pattern and minor cracks between each pair of major ones can be observed. With a temperature variation of 250 °C, the four initial cracks propagated to the borders of the ROI, and the minor cracks had grown and became visually evident, also, new minors appeared. It is essential to highlight that while the maximum principal strain field shows several cracks in the matrix, the radial displacement field (Figure 8) does not show relevant disturbances. This aspect allows the analytical model proposed in this paper to fit the experimental radial displacement and identify the model parameters.

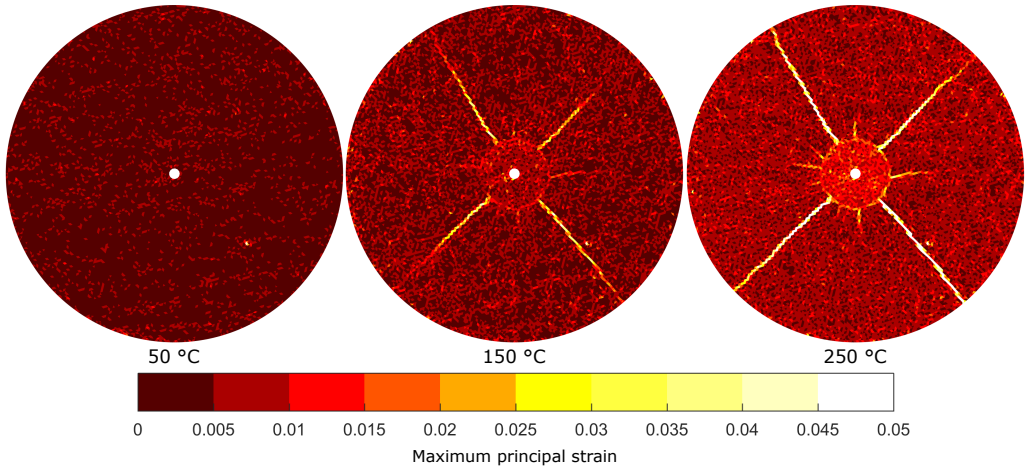

Figure 9: Evolution of the maximum principal strain field (ε_1) for temperature variations of 50, 150 and 250 °C.

The experimental results were fitted to the analytical model shown in section 3 for each temperature, as the radial displacement field in Figure 8 approximates an axisymmetric distribution. A parameter identification using a least-square fitting model was performed for the radial displacement experimental data in two steps. First, the parameter A_i is identified for the radial displacement of the inclusion domain according to equation 4. Then the parameter A_m is identified for the matrix domain according to equation 4, replacing $\frac{B_m}{r}$ by $\frac{(A_i - A_m)r_i^2}{r}$, where A_m is imposed to be smaller than A_i, and B_m is computed according to equation 8. In Figure 10, it can be seen the experimental radial displacements for each mesh node versus its radius for $\Delta T = 50, 150$ and 250 °C as point clouds and the curves of the fitted parameters for the respective temperatures. The nodal displacements close to the inner and outer mesh edges were disregarded during the identification procedure, due to higher uncertainty in these nodes caused by the lack of gray values around these nodes.

The results shown good agreement between the experimental data and the fitted model, considering that the fitted model remains inside the cloud of points. However, some issues interfere with a better adjustment of the model to the data. One of these issues is the out-of-plane displacement caused by the expansion of the sample holder supporting rods, which produces a parasite expansion in the results. Also, the analytical model does not consider discontinuities in the medium as the appearance of cracks. At last, heat hazes in the oven atmosphere create optical distortions that also contributes to oscillations.

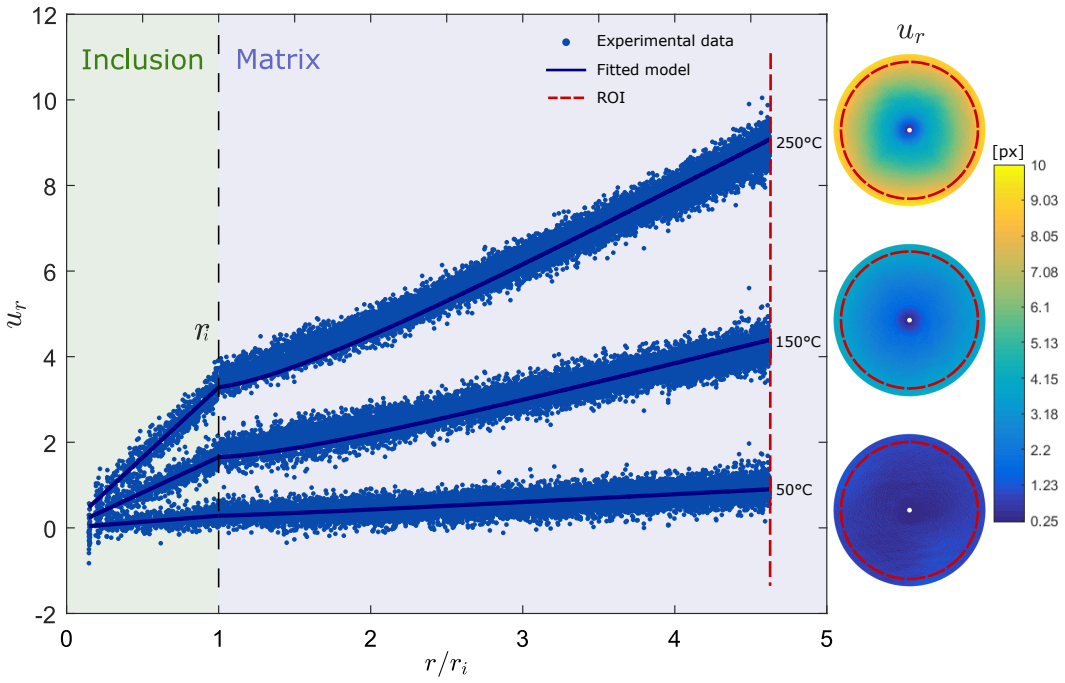

Figure 10: Radial displacement for three temperature variations, where r/r_i is the radial distance from the center of the inclusion divided by the inclusion's radius. In the right are displayed the radial displacement fields correspondent to each temperature variation. The analytical model presented is used to fit the experimental data.

To verify the feasibility of the model fitting, a comparison between the alumina mortar thermal strain obtained in the dilatometry experiment and the Am parameter (equation 6) identified in the model fitting of the MCS temperature variation experiment is presented in Figure 11. The two data showed good agreement, corroborating to ensure the viability of using the analytical model to adjust the experimental data.

6.3. Evaluation of crack initiation and propagation as a function of ΔT

An elastic and thermal displacement field was obtained using the parameters discussed in Section 6.2. These displacement fields attained were derived, and the strain computed containing only thermal and elastic components, without the influence of cracks. The respective strain field components are then subtracted from the experimental strain fields, obtained directly from DIC, and an inelastic maximum principal strain field is then computed. Figure 12 shows the maximum principal strain field of the raw experimental results, the analytical model and the subtraction between them. For the new obtained inelastic strain field, a threshold (ε^*) can be defined to quantify the cracking of the system. Several works made use of a threshold strategy, using typically a value 5 times or more the standard uncertainty of measurements [33]. It can be seen threshold values of ε^* in the order of $0.6 - 1.5 \times 10^{-3}$ (*i.e.*, between 1.5 and 3 times their uncertainty level) being used in the literature to define cracks [33, 51, 52], with meshes of similar element size as used herein. However, such works were conducted with no temperature variation and in temperatures up to 70°C, in contrast with the 300°C achieved in the MCS temperature variation experiment. For the discussion hereafter, the ε^* for the MCS experiment is defined as 0.01, ten times the noise measured for the reference images

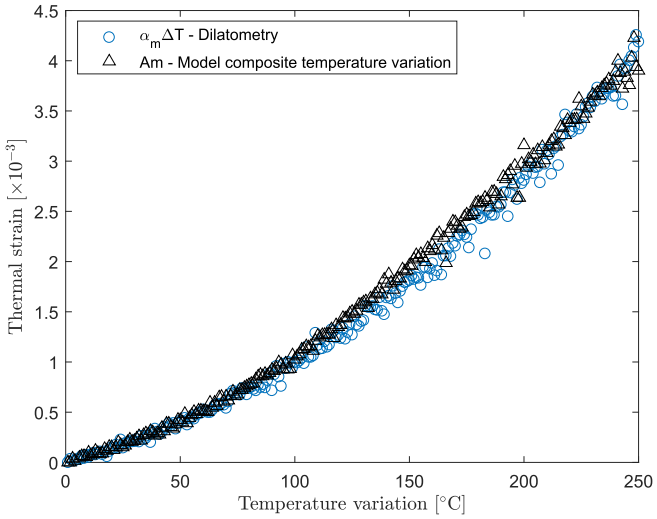

Figure 11: Comparison of $\alpha_M \, \Delta T$ obtained in the optical dilatometry test and in the analytical model fitting of the MCS temperature variation test ($A_m = \alpha_M \, \Delta T$).

(0.001). This value was selected because it did not mask the beginning of the cracking process and also did not allow noisy regions to be defined as cracks in the final results of the analysis.

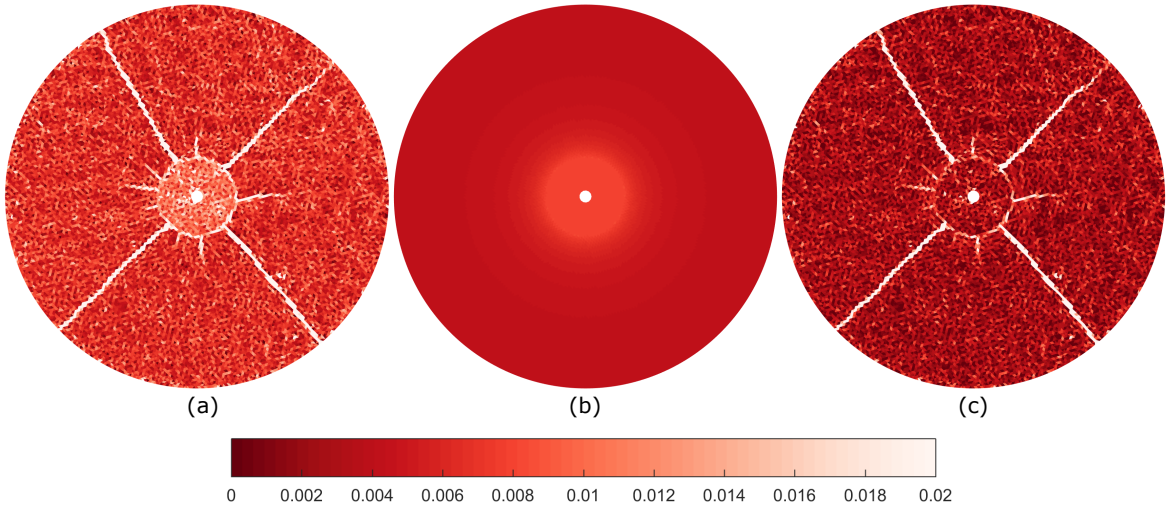

Figure 12: Post-processing to obtain an inelastic maximum principle strain field for a temperature variation of 250°C: (a) total maximum principal strain field obtained from the DIC; (b) elastic and thermal components of the maximum principal strain field obtained fitting the analytical model to the experimental results; (c) inelastic maximum principal strain field resultant of the subtraction of the thermal and elastic parcel from the total maximum principle strain field [(a) - (b)].

An evaluation of the crack initiation was performed by observing a region around the inclusion in the matrix domain to compute the percentage of elements considered as cracked (inelastic maximum principle strain ≥ 0.01) for each temperature. A temperature variation of 58°C (T = 98°C) was observed to be the critical temperature variation

where the cracking of the system initiates according to the threshold defined. The MCS was intended to produce radial cracks propagating from the interface of the inclusion and matrix, which proved successful. Figure 13 brings the percentage of elements considered cracked for each temperature.

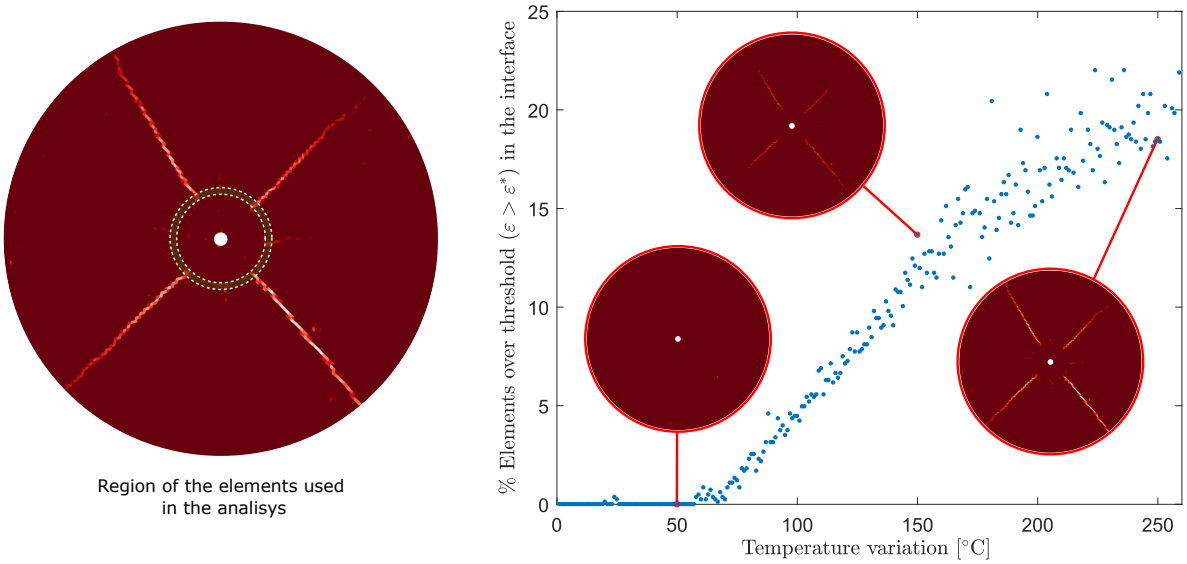

Figure 13: Analysis to evaluate the crack initiation in the model composite: (a) region containing the elements near the interface used to verify crack initiation; (b) percentage of elements surpassing the crack threshold of 0.01 for maximum principal strain for different temperature variations in a range between r_i and $r = 500$ pixels. In detail, the inelastic maximum principal strain field for the temperature variations of 50, 150 and 250 °C.

It is also possible to evaluate the crack opening and crack propagation by computing the Mean Crack Opening Displacement (MCOD) and the Surface Crack Density (SCD), respectively, during the temperature variation [32, 34]. The MCOD is computed as the maximum principal strain of the element above the threshold value multiplied by its mean element size, *i.e.* the square root of the element area. The SCD is the fraction of a given area considered cracked over the area of all elements in the region analyzed. In Figure 14 eight crack sub-regions were analyzed. They are slices of ten degrees in angle containing a max radius of 1800 pixels to avoid the results near the mesh edge. The major cracks are denoted by "×" markers, while the minor cracks by "+" markers.

The SCD results showed that the major cracks increase their propagation rate at $\Delta T \approx 75°C$ and there is a tendency to reach a plateau. For the minor cracks, there is a propagation onset at $\Delta T \approx 125°C$ and a plateau is reached at $\Delta T \approx 175°C$. This indicates that the initial cracks are protagonists of the cracking process from the beginning until the end of the test, and the appearance of new ones (a.k.a. minor cracks) do not stop their propagation. It is worth noting that the increase in oscillation of SCD values for higher ΔT is due to experimental issues as the heat haze. Major cracks also showed average MCOD values and increasing rate greater than the minor cracks, corroborating the assumption that the onset of minor cracks do not reduce the propagation of major ones.

In the executed experiments, the developed oven does not allow visualizing both sides of the tested specimens.

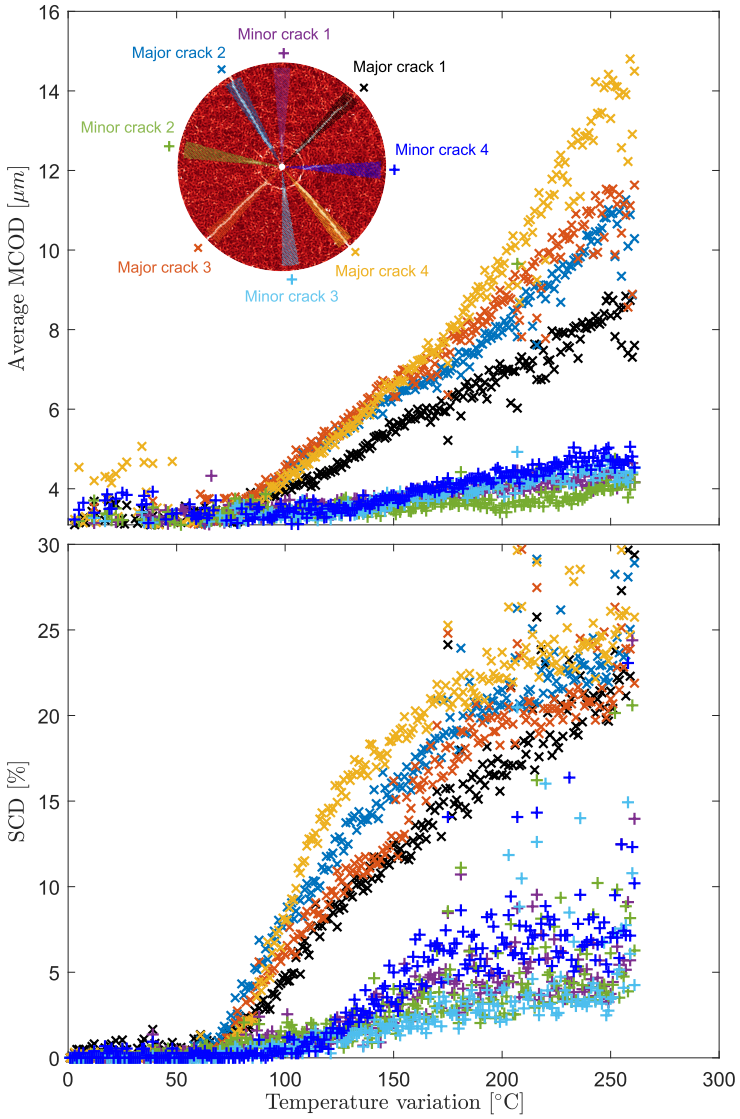

Figure 14: Average Mean Crack Opening Displacement (MCOD), expressed in μm, and Surface Crack Density (SCD), expressed in percentage (of the area that is damaged), for eight equal sized regions containing a single crack as a function of the experimental temperature variation.

Despite this experimental limitation, it is expected that the small thickness of the specimen (8 mm) contributes to achieving a similar crack path along the specimen thickness. Visual inspections of the specimen revealed the major cracks on both sides.

6.4. Multiple inclusion systems

Multiple inclusion material system presenting high local or global volume fraction are susceptible to more complex behavior. The experimental methodology of observing the cracks in model composites via DIC is also eligible to evaluate systems with multiple inclusions, however, the removing of the elastic and thermal field is a considerably harder task. The analytical solution is laborious for multiple inclusion material systems, and a numerical model would

be more interesting to represent the elastic and thermal response. Nevertheless, a simple observation of the maximum principle strain field allows observing complex crack patterns in such systems, despite the impossibility to apply the strategy presented in this paper. For the sake of illustration, an experimental result that brings a complex crack pattern resultant of the temperature variation for a high local volume fraction (*i.e.,* ≈45% considering a triangular area formed by connecting the inclusions centers) in a MCS of a cementitious mortar matrix with aluminum cylindrical inclusions can be seen in Figure 15. This result illustrates the impact of a high local volume fraction in the crack behavior of a heterogeneous system, where different crack phenomena as radial and orthoradial cracks, bifurcation of cracks, and crack coalescence can be seen. However, further analyzing such experiment remains out-of-scope of the present paper and remains as a topic for future investigations.

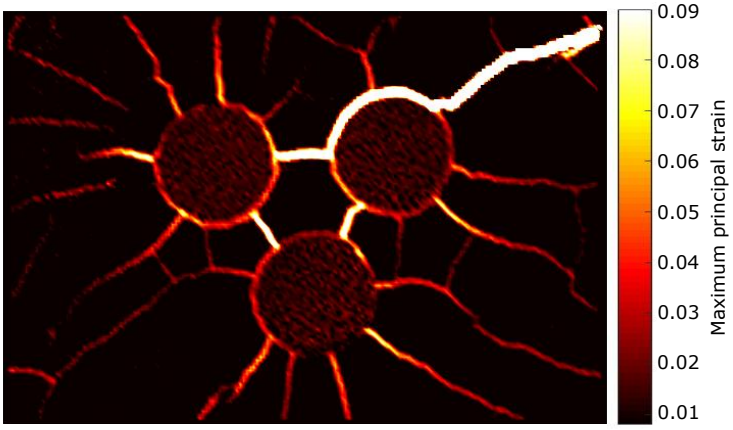

Figure 15: Crack pattern obtained via DIC for a model composite with three cylindrical aluminum inclusions in a cementitious mortar matrix for a temperature variation of $234°C$.

7. Conclusions

The proposed methodology is suitable for analyzing the interaction between the phases in a single cylindrical inclusion model composite during heating. Measurements from Digital Image Correlation (DIC) allowed to analyze the phases' interaction and to fit the experimental data to an analytical model. The crack pattern evolution was quantitatively evaluated by computing the average Mean Crack Opening Displacement (MCOD) for damaged elements and the Surface Crack Density (SCD).

An analytical model described the radial displacement for the model composite, showing good agreement with the experimental results, even for temperatures where cracks had already appeared. This correspondence is supported by the close values obtained from parameter A_m in the model fitting and the thermal strain attained from the alumina mortar's optical dilatometry. From the analysis of the interface region, it was possible to estimate the beginning of cracking in the system using a threshold value applied to the inelastic maximum principal strain field.

The present study brought new approaches to studying material phases' interaction due to CTE mismatch and the evaluation of cracking in such systems. Also, it reveals a whole field of possibilities to explore by conducting in situ

experiments using field measurement techniques allied with analytical and numerical approaches. Further, MCS with different configurations of multiple inclusions is a perspective to extrapolate the experimental study of CTE mismatch by applying methodologies such as those used in this work and using computational finite element models. The main results of this research can be summarized as:

- Development of an experimental methodology that produces in-situ full-field data of the interaction between inclusion and matrix during a temperature variation;
- Identification of experimental elastic and thermal strains by fitting an analytical model;
- Identification of an inelastic maximum principal strain field that allows to establish a threshold value to quantify the cracking evolution via the Average MCOD and SCD parameters;
- Evaluation of the crack initiation and propagation of the MCS, with perspectives to apply an analogous methodology to systems with multiple inclusions.

In future works, it is intended to evaluate the elastic properties of the materials phases for different temperatures. With these data, it is possible to estimate the interfacial stress using the analytical model and to obtain the matrix fracture stress during the experiment. The out-of-plane effects can be dealt with using a telecentric lens. Another strategy relies on two cameras acquiring images of both opposite faces of the tested specimens, which allows the obtaining of free parasite out-of-plane displacements by using the mean of these results.

8. Acknowledgments

This study was financed in part by the Coordenação de Aperfeiçoamento de Pessoal de Nível Superior - Brasil (CAPES) - Finance Code 001. The authors also acknowledge the scholarship processes 309266/2022-0, 140250/2020-4 and 168785/2017-0 from CNPq (National Council for Scientific and Technological Development, Brazil). The authors also acknowledge the financial support to carry out part of this work and grants #2020/08077-6 and #2018/23081-0, São Paulo Research Foundation (FAPESP). The authors would also like to thank François Hild for providing access to the Correli 3.0 framework.

References

[1] F. C. Campbell, Introduction to Composite Materials, 2010.

[2] M. F. Ashby, Materials Selection in Mechanical Design, Design 624doi:10.1016/B978-1-85617-663-7.00011-4.

[3] F. L. Schiavon, H. Zanardi, I. P. Zago, R. A. Angélico, Prediction of elastic parameters of particle reinforced composites using finite element simulations, Materials Research 26 (2023) e20220475. doi:https://doi.org/10.1590/1980-5373-MR-2022-0475.

[4] J. Selsing, Internal Stresses in Ceramics, Journal of the American Ceramic Society 44 (8) (1961) 419–419. doi:10.1111/j.1151-2916.1961.tb15475.x.

[5] F. C. Serbena, E. D. Zanotto, Internal residual stresses in glass-ceramics: A review, Journal of Non-Crystalline Solids 358 (6-7) (2012) 975–984. doi:10.1016/j.jnoncrysol.2012.01.040.

[6] R. W. Davidge, T. D. Green, The Strength of Two-Phase Ceramic/Glass Materials, Journal of Materials Science 3 (1968) 629–634. doi:doi.org/10.1007/BF00757910.

[7] E. S. Folias, M. Hohn, Predicting crack initiation in composite material systems due to a thermal expansion mismatch, International Journal of Fracture 93 (1-4) (1998) 335–349. doi:10.1023/A:1017160807854.

[8] L. Shen, Q. Ren, N. Xia, L. Sun, X. Xia, Mesoscopic numerical simulation of effective thermal conductivity of tensile cracked concrete, Construction and Building Materials 95 (2015) 467–475. doi:10.1016/j.conbuildmat.2015.07.117.

[9] L. Shen, Q. Ren, L. Zhang, Y. Han, G. Cusatis, Experimental and numerical study of effective thermal conductivity of cracked concrete, Construction and Building Materials 153 (2017) 55–68. doi:10.1016/j.conbuildmat.2017.07.038.

[10] M. N. Vu, S. T. Nguyen, M. H. Vu, A. M. Tang, V. T. To, International Journal of Heat and Mass Transfer Heat conduction and thermal conductivity of 3D cracked media 89 (2015) 1119–1126. doi:10.1016/j.ijheatmasstransfer.2015.05.113.

[11] J. L. Bobet, J. Lamon, Thermal Residual Stresses in Ceramic Matrix Composites- I. Axixymmetrical Model and Finite Element Analysis, Acta Metall. Mater. 43 (6) (1995) 2241–2253.

[12] N. Tessier-Doyen, J. C. Glandus, M. Huger, Untypical Young's modulus evolution of model refractories at high temperature, Journal of the European Ceramic Society 26 (3) (2006) 289–295. doi:10.1016/j.jeurceramsoc.2004.10.028.

[13] S. Jiménez-Alfaro, D. Leguillon, Modelling of glass matrix composites by the coupled criterion and the matched asymptotic approach. the effect of residual stresses and volume fraction, Theoretical and Applied Fracture Mechanics (2023) 104112doi:https://doi.org/10.1016/j.tafmec.2023.104112.

[14] B. Peng, M. Feng, J. Fan, Study on the crack–inclusion interaction with coupled mechanical and thermal strains, Theoretical and Applied Fracture Mechanics 75 (2015) 39–43. doi:https://doi.org/10.1016/j.tafmec.2014.10.006.

[15] I. Khlifi, O. Pop, J.-C. Dupré, P. Doumalin, M. Huger, Fracture process analysis in magnesia-hercynite refractory materials by combining an enhanced digital image correlation method with wedge splitting test, Theoretical and Applied Fracture Mechanics 116 (2021) 103134. doi:https://doi.org/10.1016/j.tafmec.2021.103134.

[16] D. André, B. Levraut, N. Tessier-Doyen, M. Huger, A discrete element thermo-mechanical modelling of diffuse damage induced by thermal expansion mismatch of two-phase materials, Computer Methods in Applied Mechanics and Engineering 318 (2017) 898–916. doi:10.1016/j.cma.2017.01.029.

[17] X. Wang, X. Gao, Z. Zhang, L. Cheng, H. Ma, W. Yang, Advances in modifications and high-temperature applications of silicon carbide ceramic matrix composites in aerospace: A focused review, Journal of the European Ceramic Society 41 (9) (2021) 4671–4688. doi:10.1016/j.jeurceramsoc.2021.03.051.
URL https://doi.org/10.1016/j.jeurceramsoc.2021.03.051

[18] S. T. Gonczy, Federal Aviation Administration (FAA) airworthiness certification for ceramic matrix composite components in civil aircraft systems, in: MATEC Web of Conferences, Vol. 29, 2015, pp. 1–10. doi:10.1051/matecconf/20152900002.

[19] X. Zhang, Y. Chen, J. Hu, Recent advances in the development of aerospace materials, Progress in Aerospace Sciences 97 (August 2017) (2018) 22–34. doi:10.1016/j.paerosci.2018.01.001.
URL https://doi.org/10.1016/j.paerosci.2018.01.001

[20] L. Li, Y. Liu, Y. Wang, Estimate constituent properties of 3D needle-punched C/SiC composites from hysteresis loops, International Journal of Fatigue 170 (December 2022) (2023) 107543. doi:10.1016/j.ijfatigue.2023.107543.
URL https://doi.org/10.1016/j.ijfatigue.2023.107543

[21] J. L. Bobet, R. Naslain, A. Guette, N. Ji, J. L. Lebrun, Thermal residual stresses in ceramic matrix composites-II. Experimental results for model materials, Acta Metallurgica Et Materialia 43 (6) (1995) 2255–2268. doi:10.1016/0956-7151(94)00430-7.

[22] L. Li, A micromechanical crack opening displacement model for fiber-reinforced ceramic-matrix composites considering matrix fragmentation, Theoretical and Applied Fracture Mechanics 112 (December 2020) (2021) 102875. doi:10.1016/j.tafmec.2020.102875.
URL https://doi.org/10.1016/j.tafmec.2020.102875

[23] L. Li, Hysteresis-based approach to estimate constituent properties of SiC/SiC ceramic matrix composites, International Journal of Fatigue 167 (PA) (2023) 107302. doi:10.1016/j.ijfatigue.2022.107302.
URL https://doi.org/10.1016/j.ijfatigue.2022.107302

[24] J. E. King, Failure in composite materials, Metals and Materials 5 (12) (1989) 720–726.

[25] H. J. Hoh, Z. M. Xiao, J. Luo, Crack tip opening displacement of a Dugdale crack in a three-phase cylindrical model composite material, International Journal of Engineering Science 49 (6) (2011) 523–535. doi:10.1016/j.ijengsci.2011.01.004.

[26] Y. F. Fu, Y. L. Wong, C. A. Tang, C. S. Poon, Thermal induced stress and associated cracking in cement-based composite at elevated temperatures - Part I: Thermal cracking around single inclusion, Cement and Concrete Composites 26 (2) (2004) 99–111. doi:10.1016/S0958-9465(03)00086-6.

[27] Y. F. Fu, Y. L. Wong, C. A. Tang, C. S. Poon, Thermal induced stress and associated cracking in cement-based composite at elevated temperatures - Part II: Thermal cracking around multiple inclusions, Cement and Concrete Composites 26 (2) (2004) 113–126. doi:10.1016/S0958-9465(03)00087-8.

[28] C.-H. Hsueh, P. F. Becher, Residual thermal stresses in ceramic composites . Part I : with ellipsoidal inclusions 212 (1996) 22–28.

[29] T. C. Lu, J. Yang, Z. Suo, A. G. Evans, R. Hecht, R. Mehrabian, Matrix cracking in intermetallic composites caused by thermal expansion mismatch, Acta Metallurgica Et Materialia 39 (8) (1991) 1883–1890. doi:10.1016/0956-7151(91)90157-V.

[30] I. P. Zago, R. B. Canto, R. A. Angélico, Crack pattern of a composite model material submitted to a temperature increase assisted by DIC, in: 5th Brazilian Conference on Composite Materials – BCCM 5, 2021, pp. 1–7.

[31] R. Vargas, J. Neggers, R. B. Canto, J. Rodrigues, F. Hild, Analysis of wedge splitting test on refractory castable via integrated dic, Journal of the European Ceramic Society 36 (16) (2016) 4309 – 4317.

[32] V. F. Sciuti, F. Hild, V. C. Pandolfelli, T. Santos, B. Smaniotto, R. B. Canto, Digital Image Correlation applied to in situ evaluation of surface cracks upon curing of MgO-containing refractory castables, Journal of the European Ceramic Society (2020).

[33] V. F. Sciuti, R. Vargas, R. B. Canto, F. Hild, Pyramidal adaptive meshing for Digital Image Correlation dealing with cracks, Engineering Fracture Mechanics 256 (2021) 107931. doi:10.1016/j.engfracmech.2021.107931.

[34] V. F. Sciuti, R. Vargas, R. B. Canto, F. Hild, Modal characterization of crack network development in an mgo containing refractory castable, The Journal of Strain Analysis for Engineering Design 58 (6) (2023) 490–500. doi:10.1177/03093247221141490.

[35] M. A. Sutton, W. J. Wolters, W. H. Peters, W. F. Ranson, S. R. McNeill, Determination of displacements using an improved digital correlation method, Image and Vision Computing 1 (3) (1983) 133 – 139. doi:10.1016/0262-8856(83)90064-1.

[36] N. McCormick, J. Lord, Digital image correlation, Materials Today 13 (12) (2010) 52–54. doi:10.1016/S1369-7021(10)70235-2.

[37] F. Hild, S. Roux, Digital Image Correlation, Wiley-VCH, Weinheim (Germany), 2012, pp. 183–228.

[38] F. S. Montilha, F. O. Rocco, C. C. Melo, V. F. Sciuti, R. B. Canto, Identification of dilatancy in green compacted ceramic powder via digital image correlation, Powder Technology 330 (May) (2018) 471–476. doi:10.1016/j.powtec.2018.01.037.

[39] Y. Joliff, J. Absi, J. C. Glandus, M. Huger, N. Tessier-Doyen, Experimental and numerical study of the thermomechanical behaviour of refractory model materials, Journal of the European Ceramic Society 27 (2-3) (2007) 1513–1520. doi:10.1016/j.jeurceramsoc.2006.04.031.

[40] Y. Joliff, J. Absi, M. Huger, J. C. Glandus, Microcracks with unexpected characteristics induced by CTE mismatch in two-phase model materials, Journal of Materials Science 43 (2007) 330–337. doi:10.007/s10853-007-1691-x.

[41] B. Luchini, V. F. Sciuti, R. A. Angélico, R. B. Canto, V. C. Pandolfelli, Thermal expansion mismatch inter-inclusion cracking in ceramic systems, Ceramics International 42 (10) (2016) 12512–12515. doi:10.1016/j.ceramint.2016.05.013.

[42] Y. Joliff, J. Absi, J. C. Glandus, M. Huger, N. Tessier-Doyen, Experimental and numerical study of the thermomechanical behaviour of refractory model materials, Journal of the European Ceramic Society 27 (2-3) (2007) 1513–1520.

[43] H. Leclerc, J. Neggers, F. Mathieu, S. Roux, F. Hild, Correli 3.0, IDDN.FR.001.520008.000.S.P.2015.000.31500 (2015).

[44] G. Besnard, F. Hild, S. Roux, "Finite-Element" displacement fields analysis from digital images: Application to Portevin-Le Chatelier bands, Experimental Mechanics 46 (6) (2006) 789–803.

[45] P. Leplay, O. Lafforgue, F. Hild, Analysis of asymmetrical creep of a ceramic at 1350c by digital image correlation, Journal of the American Ceramic Society 98 (7) (2015) 2240–2247. doi:https://doi.org/10.1111/jace.13601.

[46] Y. Liu, L. Yu, Z. Wang, B. Pan, Neutralizing the impact of heat haze on digital image correlation measurements via deep learning, Optics and Lasers in Engineering 164 (February) (2023) 107522. doi:10.1016/j.optlaseng.2023.107522.

[47] R. Vargas, X. Pinelli, B. Smaniotto, F. Hild, R. B. Canto, On the effect of sintering temperature on the fracture energy of an Alumina-Mullite-Zirconia castable at 600C, Journal of the European Ceramic Society 41 (7) (2021) 4406–4418. doi:10.1016/j.jeurceramsoc.2021.01.023.

[48] X. Zhang, C. Li, L. Yu, B. Pan, Heatwave distortion correction using an improved reference sample compensation method and multispectral digital image correlation, Appl. Opt. 60 (13) (2021) 3716–3723. doi:10.1364/AO.420124.

[49] V. F. Sciuti, R. B. Canto, J. Neggers, F. Hild, On the benefits of correcting brightness and contrast in global digital image correlation: Monitoring cracks during curing and drying of a refractory castable, Optics and Lasers in Engineering 136 (2021) 106316.

[50] M. Sutton, J. Yan, V. Tiwari, H. Schreier, J. Orteu, The effect of out-of-plane motion on 2d and 3d digital image correlation measurements, Optics and Lasers in Engineering 46 (10) (2008) 746–757. doi:https://doi.org/10.1016/j.optlaseng.2008.05.005.

[51] V. F. Sciuti, F. Hild, V. C. Pandolfelli, T. Santos, B. Smaniotto, R. B. Canto, Digital Image Correlation applied to in situ evaluation of surface cracks upon curing of MgO-containing refractory castables, Journal of the European Ceramic Society 41 (1) (2021) 1003–1014. doi:10.1016/j.jeurceramsoc.2020.04.055.

[52] V. F. Sciuti, R. Vargas, N. Guerrero, M. E. Marante, F. Hild, Digital image correlation analyses of masonry infilled frame: Uncertainty-based mesh refinement and damage quantification, Mathematics and Mechanics of Solids 0 (0) (2023). doi:10.1177/10812865231174840.